Analytica Chimica Acta 1274 (2023) 341541

Contents lists available at ScienceDirect

Analytica Chimica Acta

journal homepage: www.elsevier.com/locate/aca

# Type-I heterojunction destruction by *In situ* formation of $Bi_2S_3$ for split-type photoelectrochemical aptasensor

Xue Dong [a], Hanyu Wang [a], Xiang Ren [a], Hongmin Ma [a], Dawei Fan [a], Dan Wu [a,*], Qin Wei [a], Huangxian Ju [a,b]

[a] Key Laboratory of Interfacial Reaction & Sensing Analysis in Universities of Shandong, School of Chemistry and Chemical Engineering, University of Jinan, Jinan, 250022, PR China

[b] State Key Laboratory of Analytical Chemistry for Life Science, College of Chemistry and Chemical Engineering, Nanjing University, Nanjing, 210023, PR China

## HIGHLIGHTS

- MSNs-assisted PEC aptasensor is constructed to detection of PSA.
- BiOI/BiOBr destruction by *in situ* formation of $Bi_2S_3$ causes signal quencher.
- The controlled-release strategy effectively ensures biological activity.

## GRAPHICAL ABSTRACT

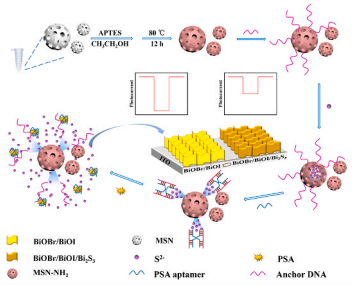


## ARTICLE INFO

Handling Editor: Dr Jing-Juan Xu

*Keywords:*
MSNs
*In situ* formation
BiOI/BiOBr/$Bi_2S_3$
PSA
Controlled-release system

## ABSTRACT

Development of new strategies in photoelectrochemical (PEC) sensors is an important way to realize sensitive detection of biomolecule. In this study, mesoporous silica nanospheres (MSNs)-assisted split-type PEC aptasensor with *in situ* generation of $Bi_2S_3$ was proposed to achieve reliable detection of prostate-specific antigen (PSA). To be more specific, this bioresponsive release system will release large amounts of $Na_2S$ by the reaction between PSA and aptamer that capped $Na_2S$-loading MSNs. Next, the $Na_2S$ reacts with Bi to yield BiOI/BiOBr/$Bi_2S_3$ composite, which leads to an alteration in the electron-hole transfer pathway of the photoelectric material and a decrease in the response. As the PSA concentration increases, more $Na_2S$ can be released and lower photocurrent is obtained. The linear range under the optimal experimental conditions is 10 pg·mL$^{-1}$-1 μg·mL$^{-1}$, and the detection limit is 1.23 pg·mL$^{-1}$, which has satisfactory stability and anti-interference.

## 1. Introduction

The combination of photoelectrochemical (PEC) methods and biosensing technologies, as a prospective analytical tool, has been gaining more and more attention resulting from its fascinating characteristics of simple equipment, cost-effectiveness and high sensitivity over the years [1–6].

The selection of photoelectric materials is essential to improve the sensitivity of sensor [7–10]. Bismuth oxyhalide (BiOX, X = Cl, Br and I), a new model of layered oxide semiconductor, was extensively utilized in

* Corresponding author.
*E-mail address:* wudan791108@163.com (D. Wu).

https://doi.org/10.1016/j.aca.2023.341541
Received 27 April 2023; Received in revised form 7 June 2023; Accepted 16 June 2023
Available online 23 June 2023

the field of photoelectrochemistry [11–13]. However, it can be led to the high electron-hole pairs recombination rate when BiOX is used alone [14–16]. Therefore, BiOX always combines with other photoelectric materials, such as $WO_3$/BiOI/CdS [17], AgI/Ag/BiOI Z-scheme heterojunction arrays [18], Bi/BiOBr/$TiO_2$ [19] and AgNP/BiOCl [20]. In view of this, BiOI/BiOBr type-I heterostructure was prepared through the one-pot method. BiOI and BiOBr with similar microstructure can efficiently avoid the recombination of photogenerated electron-hole, thus further improving its photoelectric performance.

Another important process in PEC sensing is biological recognition [21–24]. The majority of conventional PEC biosensing platforms like the label-free type as well as the sandwich type, the procedure of the biological recognition happens straightway on the electrodes [25,26]. On the one hand, the modification process of electrodes in these strategies is extremely sophisticated and full of uncertainties. On the other hand, the presence of metals in photoelectric material may inactivate immune substances to a certain extent and further lead to a decrease in the sensitivity [27–29]. To address the above problems, some PEC sensing strategies that separate the immune response and electrode modification have been investigated and shown to be well-designed and operable. For

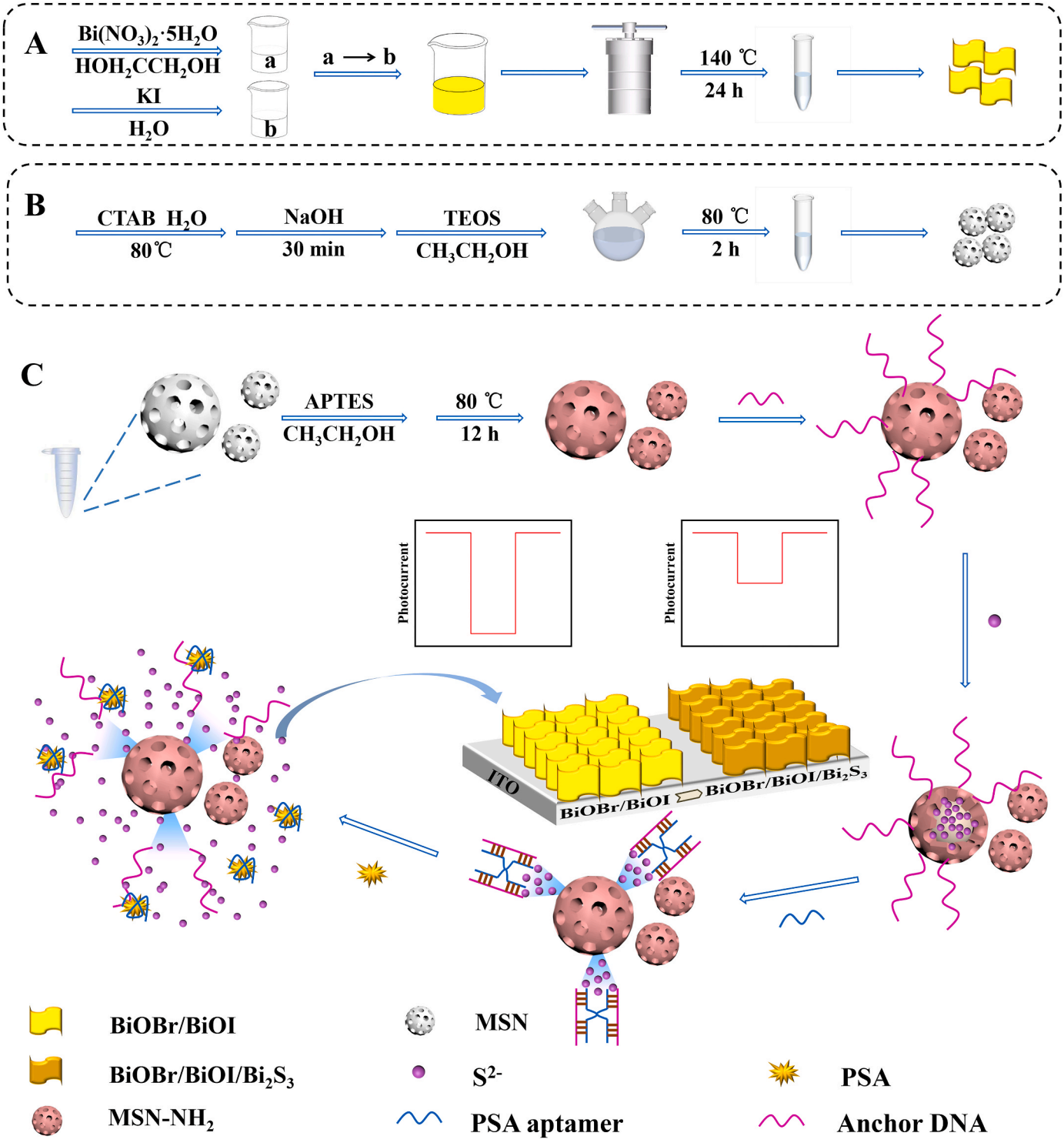


**Scheme 1.** The preparation of (A) BiOBr/BiOI and (B) MSN. (C) Fabrication process of the PEC aptasensor.

example, Gao et al. designed a liposome-assisted *in situ* generation of new heterostructure for signal quenching to achieve sensitive detection of h-FABP [30]. Li et al. achieved high-throughput signal analysis of lysozyme with the direct introduction of electron donors in electrolyte assisted by mesoporous silica nanospheres (MSNs) loaded with dopamine [31]. Although some progress has been accomplished, new strategies based on split-type PEC sensing platforms need to be explored in depth.

All in all, based on the above ideas, this work proposed a new detection mode: the relationship between the output current and the target concentration will be revealed by destroying the original energy-matched heterojunction through *in situ* generation of $Bi_2S_3$ with the assistance of MSNs. In particular, indium-tin oxide (ITO)/BiOBr/BiOI was prepared as working electrode, as exhibited in Scheme 1. BiOBr/BiOI as energy-matched type-I heterojunction under visible light irradiation can generate large photocurrent. In addition, the MSNs loaded with $Na_2S$ are blocked by the PSA aptamer chain and anchor-DNA. In the absence of PSA, the blocked MSNs will not be opened and $Na_2S$ will continue to exist in the MSNs without significant changes in photocurrent. When PSA is present, it will specifically bind to the aptamer chain causing the MSNs to be opened while releasing $Na_2S$ that reacts with Bi on the ITO/BiOBr/BiOI electrode *in situ* to form BiOBr/BiOI/$Bi_2S_3$ [32,33]. Because the conduction band (CB) and valence band (VB) of $Bi_2S_3$ are higher than those of BiOI, after being excited by light, electrons in the CB of $Bi_2S_3$ are more inclined to transfer towards the CB of BiOI, resulting in a decrease in the number of electrons that occurs reduction reactions on the electrode surface. To sum up, the original heterojunction is destroyed causing the quenching of the photocurrent. Thus, the obtained photocurrent signal will reveal the specific recognition, which can be used for quantitative determination of PSA: higher concentrations of PSA will release more $Na_2S$ and thus obtain a lower signal response. This work demonstrates the important potential of generating new compounds by *in situ* growth to destroy the original perfect heterostructure under MSNs-assisted and thus leads to the output signal change in PEC analysis. It may provide new thoughts for the design of advanced PEC sensors in the future.

## 2. Experimental section

### 2.1. Preparation of BiOBr/BiOI

A hydrothermal method was used to prepare BiOBr/BiOI on the basis of a previous literature [16]. The details were presented in Supplementary Material.

### 2.2. Preparation of MSNs and amino-functionalized MSNs

About the preparation of MSNs [34], 0.5000 g CTAB and 240 mL ultrapure water were added to 500 mL flask, which heated to 80 °C and stirred until CTAB was completely dissolved. Then 6 mL 0.5 mol·$L^{-1}$ NaOH was slowly added to the above solution, maintained for 30 min, after which added a mixture of 2.5 g tetraethyl silicate (TEOS) and 5 g anhydrous ethanol. Holding for 2 h after precipitation occurred, then cooled it naturally and washed the above products with a mixed solvent of anhydrous ethanol/ultrapure water, and dried overnight at 60 °C. After sufficient grinding with a mortar, the products were calcined at a temperature increase rate of 1 °C·$min^{-1}$ to 550 °C for 5 h.

For the amination of MSNs [35], 0.2400 g $SiO_2$ and 240 μL (3-aminopropyl) triethoxysilane (APTES) were refluxed in 12 mL anhydrous ethanol at 80 °C for 12 h. The MSNs was centrifuged at 12,000 r and cleaned with ultrapure water. After cooling at room temperature, the products were dried to obtain the MSNs-$NH_2$.

### 2.3. Preparation of DNA-modified MSNs and $Na_2S$ blocking

A conventional method was used to prepare the DNA-modified MSNs [35,36]. The specific preparation steps were shown in Supplementary Material. The as-obtained DNA-modified MSNs was centrifuged, followed by a washing step with ultrapure water to remove excessive anchor-DNA, and the resulting product was distributed in 500 μL pH 7.4 0.1 mol·$L^{-1}$ phosphate buffered saline (PBS) for subsequent utilization. Subsequently, $Na_2S$ was added to the above solution so that the final concentration of $Na_2S$ was 2.0 mol·$L^{-1}$ and shaken for 24 h to load $Na_2S$ into the DNA-modified MSNs. Following, $Na_2S$ was blocked by adding 50 μL 200 μmol·$L^{-1}$ PSA aptamer and incubated at 37 °C for 8 h. The $Na_2S$-loaded MSNs were centrifuged, washed with ultrapure water at 15,000 r and scattered in 500 μL pH 7.4 PBS. Ultimately, the product was placed at 4 °C for further use.

### 2.4. Fabrication process of the sensor and PEC measurements

70 μL pH 7.4 PBS was used to dilute 20 μL $Na_2S$-loaded MSNs and 10 μL PSA at different concentrations was added for releasing the $S^{2-}$. The sulotion was shaken for 4 h, then the supernatant was collected. For the PEC electrode part, 10 μL 6·mg $mL^{-1}$ well-dispersed BiOI/BiOBr solution was dropped onto ITO conductive glass. After natural drying, 10 μL the above supernatant was added dropwise onto ITO/BiOI/BiOBr electrode, followed by repeated washing with ultrapure water after natural drying to obtain the PSA concentration-dependent ITO/BiOI/BiOBr/$Bi_2S_3$ working electrode [32,33].

Using a LED white light lamp (100 W), the PEC signals were recorded under illumination by electrochemical workstation. For experiment part, a conventional three-electrode system was applied in 0.1 mol $L^{-1}$ pH 8.0 Tris-HCl: the ITO/BiOI/BiOBr/$Bi_2S_3$, Hg/$Hg_2Cl_2$ and Pt wire were chosen as the working, reference and counter electrode, respectively.

## 3. Results and discussion

### 3.1. Characterization of the amino-functionalized MSNs

The morphology of the as-synthesized MSNs was first investigated by scanning electron microscopy (SEM) and high resolution transmission electron microscopy (HRTEM). As exhibited in Fig. 1A, the majority of the prepared MSNs presented homogeneous nanostructure with a diameter of about 50 nm.

In order to connect the carboxylated anchor-DNA strands to the synthesized MSNs surface, the success of the amino-functionalized MSNs process was demonstrated by energy-dispersive X-ray (EDX) spectroscopy and Fourier transform infrared (FT-IR) spectroscopy. A uniform distribution of N, Si, O can be seen from Fig. 1B, indicating that the MSNs were successfully modified with the amino groups. The results as displayed in Fig. 1C, the MSNs before amination emerged remarkable peaks at 819 and 1097 $cm^{-1}$, corresponded to SiO–H and Si–O–Si of $SiO_2$, respectively. The FT-IR spectrum after amination shown that the N–H stretching vibrational peaks appeared at 3389 and 1557 $cm^{-1}$. The intensity of the original peak at 819 $cm^{-1}$ is not significantly increased and shifted in the direction of the small wave number. In conclusion, amino-functionalized MSNs had been successfully obtained. Moreover, nitrogen adsorption-desorption isotherms were shown in Fig. 1D. The Brunauere-Emmette-Teller (BET) specific surface area was 838.1 $m^2$ $g^{-1}$, and the most pore sizes were around 2 nm, which provided the prerequisite for the MSNs to be appropriate for loading $Na_2S$.

### 3.2. Characterization of the BiOBr/BiOI and BiOBr/BiOI/$Bi_2S_3$

Firstly, X-ray diffraction (XRD) pattern was used to identify the successfully preparation of material. As can be seen from Fig. 2A, the peaks of BiOBr/BiOI heterojunction were consistent to what was reported in previous articles [16], which demonstrated the combination of the monomers was successful. In addition, compared with alone BiOI and BiOBr, the widened peak shape is also a feature of successful

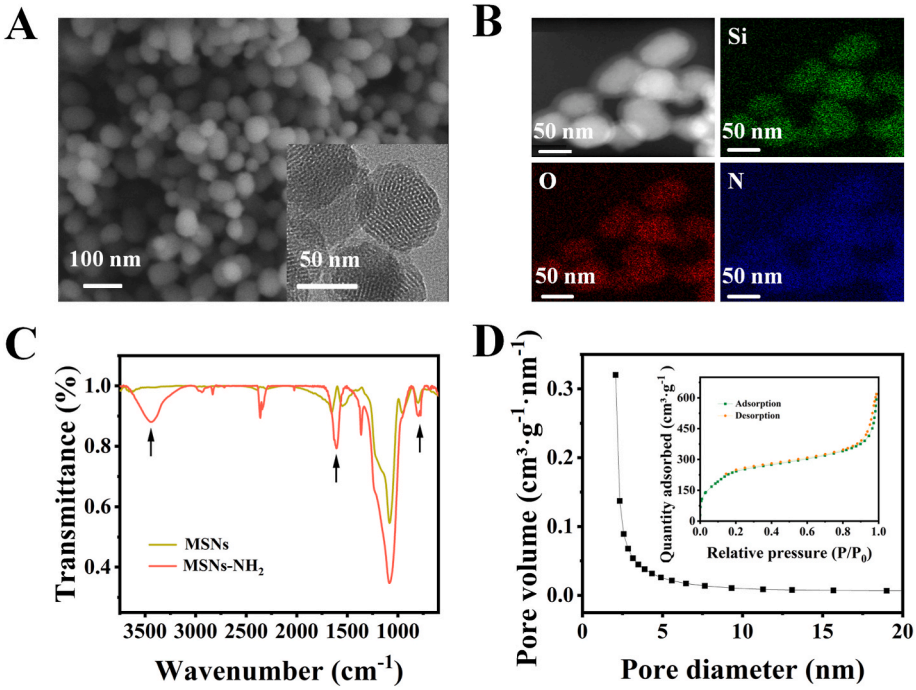


**Fig. 1.** (A) SEM and TEM image of MSNs. (B) EDX elemental mapping images of MSNs-$NH_2$. (C) FT-IR image of MSNs and MSNs-$NH_2$. (D) Pore-size distribution and nitrogen adsorption–desorption isotherms of MSNs-$NH_2$.

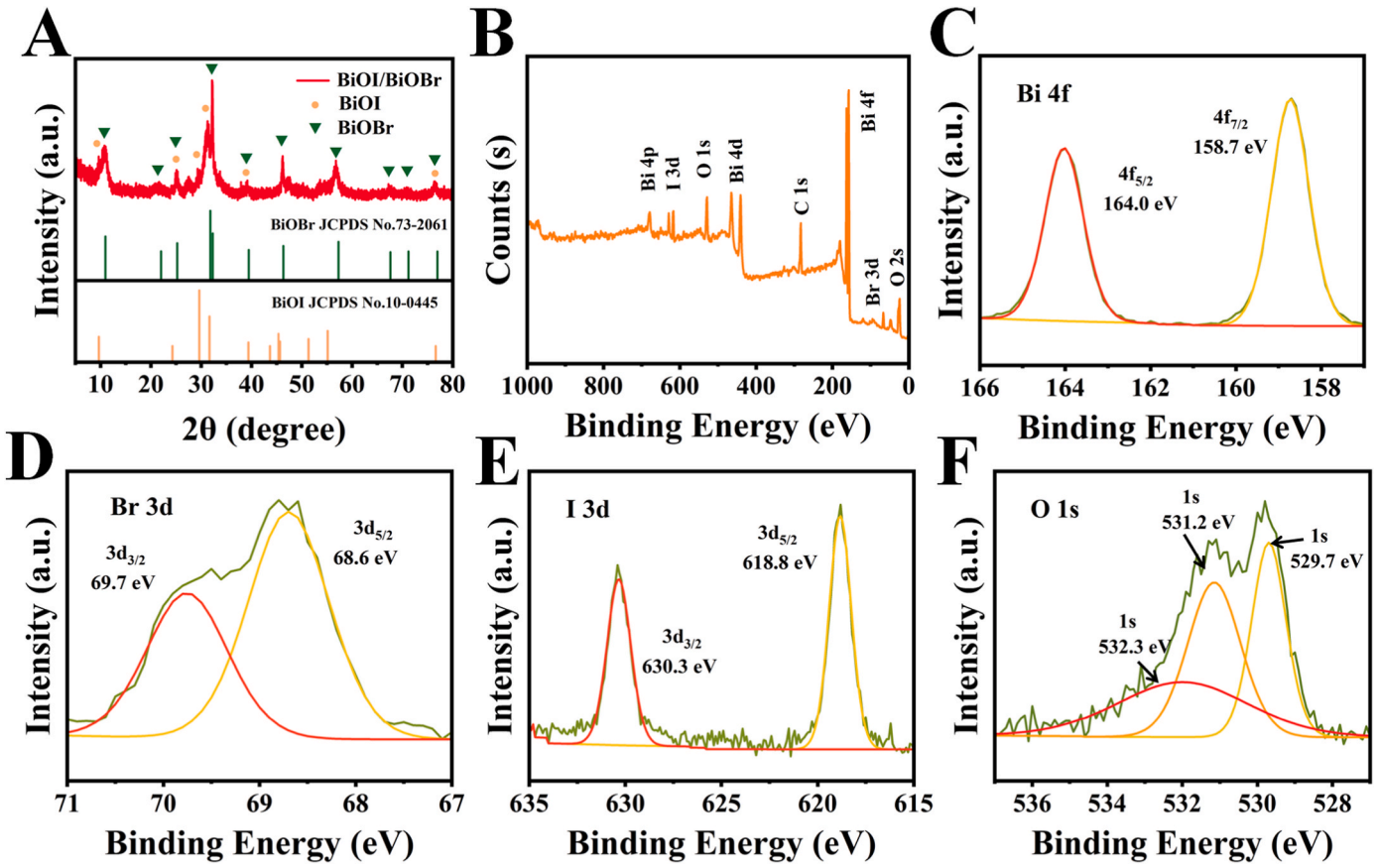


**Fig. 2.** (A) XRD image of BiOBr/BiOI. (B) XPS spectra of BiOBr/BiOI heterojunction. High-resolution XPS spectra of (C) Bi 4f (D) Br 3 d (E) I 3 d and (F) O 1s.

BiOBr/BiOI preparation [37]. To be specific, there are 6 diffraction peaks in the spectra at 9.6°, 24.3°, 29.6°, 31.6°, 39.3° and 76.6°, corresponding to (001), (101), (102), (110), (004) and (107) of BiOI (JCPDS No. 10–0445). Besides, 10 diffraction peaks appeared at 10.9°, 22.0°, 25.3°, 31.8°, 39.4°, 46.3°, 56.4°, 67.6°, 71.2° and 77.0°, which is corresponding to (001), (002), (011), (012), (112), (020), (114), (220), (124) and (130) of BiOBr (JCPDS No. 73–2061). The elemental compositions and chemical states of BiOBr/BiOI were revealed by X-ray photoelectron spectroscopy (XPS). As presented in Fig. 2B, five elements can be detected. The corresponding high-resolution XPS spectra of Bi, Br, I and O were depicted in Fig. 2C–F. The characteristic peaks, centered at 158.7 and 164.0 eV, could be attributed to Bi $4f_{7/2}$ and Bi $4f_{5/2}$, demonstrating the existence of the valence states of $Bi^{3+}$ [38]. The binding energies of 68.7, 69.7, 618.6 and 630.3 eV could be assigned to Br $3d_{5/2}$, Br $3d_{3/2}$, I $3d_{5/2}$, I $3d_{3/2}$, which confirming the existence of $Br^-$ and $I^-$ [39–41]. The O 1s peaks at 529.7 and 531.2 eV could be ascribed to the oxygen in BiOBr/BiOI lattice, and peak at 532.3 eV could be corresponded to hydroxyl adsorbed on BiOBr/BiOI surface [42,43].

The microstructure of the BiOBr/BiOI heterojunction and BiOBr/BiOI/$Bi_2S_3$ composite were studied using SEM. The BiOBr/BiOI heterojunction was synthesized by reported literature, as shown in Fig. 3B presented ultrathin nanosheet architectures [44]. This ultrathin nanosheet with large specific surface area can offer abundant adsorption/-reaction sites and facilitate light absorption, which is beneficial for the following construction of PEC aptasensor. The SEM image of BiOBr/BiOI/$Bi_2S_3$ obtained directly by the reaction of $S^{2-}$ released through MSNs with BiOBr/BiOI was shown in Fig. 3D. We can see that BiOBr/BiOI/$Bi_2S_3$ has become thicker compared to simple BiOBr/BiOI. The elemental distribution of BiOBr/BiOI and BiOBr/BiOI/$Bi_2S_3$ were investigated using EDX spectroscopy. The elemental mapping images of BiOBr/BiOI in Fig. 3A and a-d exhibited that the elements Bi, Br, O and I were uniformly distributed throughout BiOBr/BiOI. Moreover, the

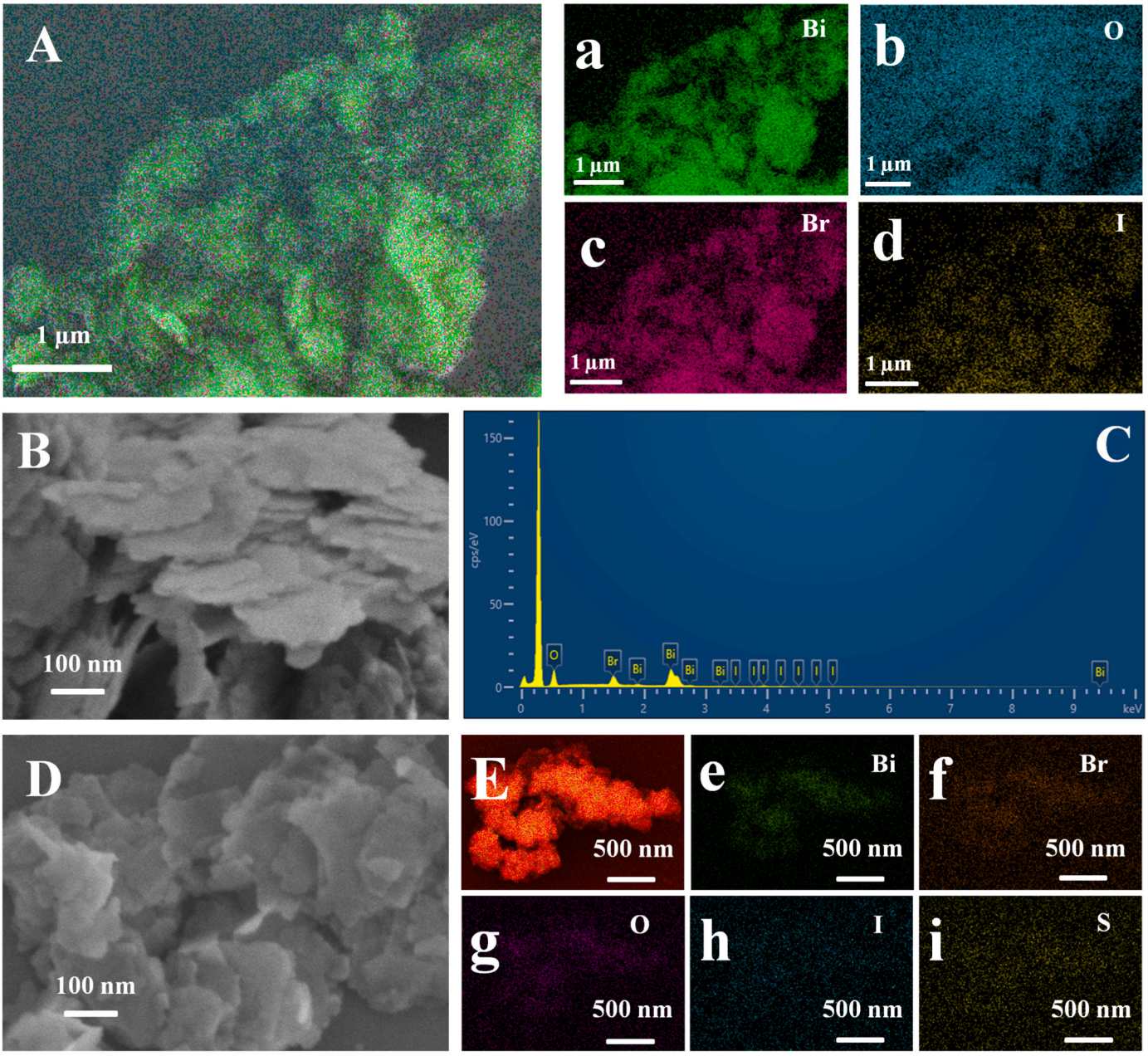


**Fig. 3.** (A) (a–d) (C) EDX elemental mapping images of BiOBr/BiOI. SEM image of (B) BiOBr/BiOI, (D) BiOBr/BiOI/$Bi_2S_3$. (E) (e–i) EDX elemental mapping images of BiOBr/BiOI/$Bi_2S_3$.

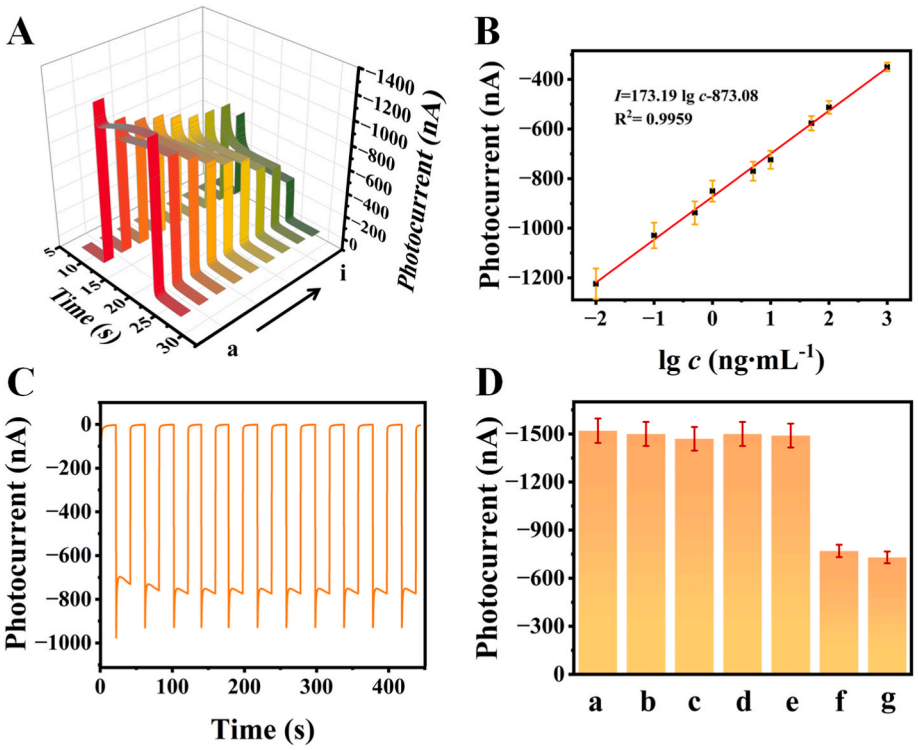


**Fig. 4.** (A) Photocurrent response and (B) the corresponding calibration curves of PSA detection: (a–i) 0.01, 0.1, 1, 5, 10, 50, 100, 1000 ng·mL$^{-1}$, respectively. (C) Stability test ($c_{PSA}$ = 5 ng·mL$^{-1}$). (D) Selectivity test: (a) Blank, 50 ng·mL$^{-1}$ (b) CEA, (c) NSE (d) BSA (e) SARS-Cov-2, (f) 5 ng·mL$^{-1}$ PSA, (g) 5 ng·mL$^{-1}$ PSA + MIX (n = 5).

element S can be observed, as shown in Fig. 3E and e-i, which may be due to the newly formed BiOBr/BiOI/$Bi_2S_3$.

### 3.3. Characterization of the PEC sensor

In order to obtain the best performance of the aptasensor, the concentration of BiOBr/BiOI and the pH of Tris-HCl were optimized, and the experimental results were shown in Fig. S1A and B, it can be seen that the maximum current can be obtained when the concentration of BiOBr/BiOI is 6 mg·mL$^{-1}$ and the pH value of the electrolyte is 8.0.

The PEC response (Fig. S2A) and the electrochemical impedance spectroscopy (EIS) (Fig. S2B) were methodically implemented to substantiate the successful fabrication of the aptasensor. ITO alone does not produce a photocurrent response when illuminated by visible light. After the BiOBr/BiOI was loaded on the electrode, a large photocurrent response was generated upon illumination due to its better energy level matching. When the $S^{2-}$ was applied to the BiOBr/BiOI surface, the signal was obviously diminished, further demonstrating that $S^{2-}$ can destroy the already well-formed heterojunction. −1400 and −770 nA were corresponding to the photocurrents of ITO/BiOBr/BiOI incubated in the release solution after identification of 0 and 10 ng·mL$^{-1}$, indicating the reduce in the photocurrent of ITO/BiOBr/BiOI to be approximately 55%. Such an obvious current decrease demonstrated the high sensitivity of the split-type PEC aptasensor. Besides, the impedances of ITO, ITO/BiOBr/BiOI, and ITO/BiOBr/BiOI/$Bi_2S_3$ tested in the $K_3[Fe(CN)_6]$ solution were, separately, exhibited in Fig. S2B. In addition, the results of incremental impedances further verified the successful constraction of the split-type PEC sensing platform.

### 3.4. Analysis of PSA and the PEC sensor performance

Based on the relationship between the current reduction and PSA concentration, a split-type signal-quenching PEC biosensing platform can be accordingly fabricated. As exhibited in Fig. 4A, the gradual decrease of photocurrent corresponded to the increasing of PSA concentration when ITO/BiOBr/BiOI reacts with MSNs releasing solution. The corresponding derived calibration curve was exhibited in Fig. 4B. In the range of 10 pg·mL$^{-1}$-1 μg·mL$^{-1}$, by the results of the measurement, the current linearly decreased with the logarithm of PSA concentrations. The linear regression equation is $I$ = 173.19 lg $c_{PSA}$−873.08, with a satisfactory correlation coefficient of $R^2$ = 0.9959. Moreover, the detection limit of constructed PEC aptasensor is 1.23 pg·mL$^{-1}$, which was compared with other reported methods for the PSA detection (Table S1). Fig. 4C exhibited the stable signal output of ITO/BiOBr/BiOI after dropping the releasing solution of 10 ng·mL$^{-1}$ of PSA under repetitive on−off illumination for 450 s. Then, other possible interference substances, such as carcinoembryonic antigen (CEA), neuron-specific enolase (NSE), bovine serum albumin (BSA) and severe acute respiratory syndrome coronavirus 2 (SARS-Cov-2), were used to explore the specificity of this aptasensor. As shown in Fig. 4D, the results exhibited insignificant changes in the signal of the PEC platform under duplicate environment. These above conclusions demonstrated that the proposed ITO/BiOBr/BiOI combined with MSNs-mediated split-type bioassay can be used for the reliable PSA detection.

### 3.5. Sample analysis

Three human serum samples were used as initial samples for standard recovery testing to prove the application of the constructed PEC aptasensor. Prior to the experiment, serum samples were centrifuged three times at 9500 r to obtain the supernatant. The concentration of PSA in the serum was 3.04 ng·mL$^{-1}$. After testing, the calculated recovery rates were located in the range of 97.0–101.4% with a low RSD from 2.4 to 3.2% (Table S2), indicating that the split-type PEC aptasensor can meet the needs of clinical PSA detecting.

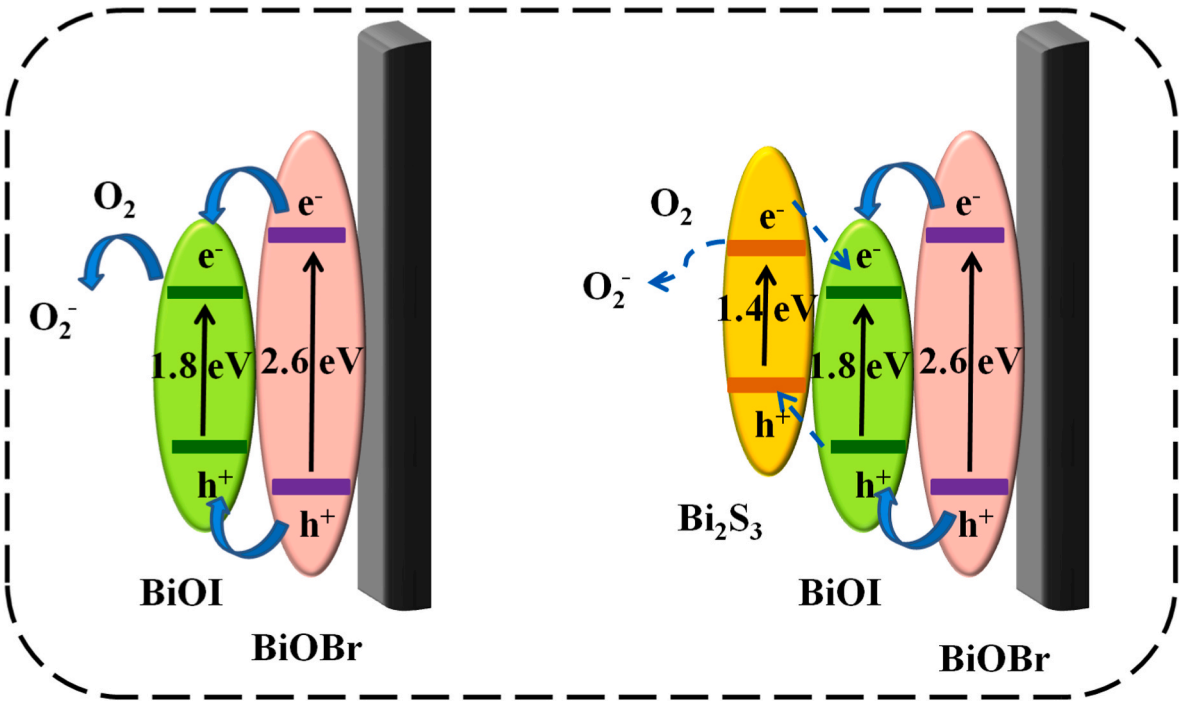


**Scheme 2.** Possible schematic mechanism of the PEC aptasensor for detecting PSA.

### 3.6. Possible mechanism of the PEC sensor

Scheme 2 illustrated the possible mechanism of the MSNs-assisted PEC aptasensor for the detection of PSA. Upon visible light irradiation, BiOBr/BiOI type-I heterojunction can generate photoexcited electron−hole pairs. Because of the perfect energy level matching, the electrons in CB of BiOBr may transfer to that of BiOI. Meanwhile, the holes in VB of BiOBr should shift to BiOI, and the potential of $O_2/O_2^-$ is −0.33 eV that is more positive than the CB of BiOI, accordingly, dissolved $O_2$ in the electrolyte will reacte with the electrons in the CB of BiOI, which contributed to produce the PEC response [45]. When PSA of various concentrations were introduced to react with the $Na_2S$-loaded MSNs for releasing the encapsulated $Na_2S$, the MSNs released products were dropped onto ITO/BiOBr/BiOI electrode, which led to the BiOBr/BiOI was extremely destroyed by $Bi_2S_3$. Because the CB and VB of $Bi_2S_3$ are higher than those of BiOI, there is a tendency for the photoexcited electrons of $Bi_2S_3$ to shift to BiOI under the illumination. Compared with the previous case without dropwise addition of the releasing solution, the electron transfer path is altered, and the reaction between the dissolved oxygen and electron becomes more difficult, and the output PEC response is subsequently weaker.

## 4. Conclusion

In summary, this study successfully constructed MSNs-assisted *in situ* growth of $Bi_2S_3$ to destroy type-I heterojunction for PEC bioassay by $Na_2S$-loaded MSNs, biorecognition in centrifugal tubes and ITO/BiOBr/BiOI photoelectrode. The $Na_2S$ released from MSNs was guided to react with BiOBr/BiOI to form the BiOBr/BiOI/$Bi_2S_3$ *in situ*. The newly *in situ* generated $Bi_2S_3$ possesses higher VB and CB than BiOI. Therefore, the transfer paths of photogenerated electron-hole pairs are altered, eventually leading to signal quenching. A new type of PEC bioassay for PSA detection can be realized with excellent analytical characteristics such as excellent reproducibility, satisfactory specificity and high sensitivity. Meanwhile, the innovative thought of using $Na_2S$-triggered perfectly matched BiOBr/BiOI heterojunction destruction to fabricate split-type platform based on a controlled-release strategy may motivate more prospective applications for advanced PEC biosensor development.

## CRediT authorship contribution statement

**Xue Dong:** Conceptualization, Data curation, Writing – original draft. **Hanyu Wang:** Methodology, Data curation, Writing – review & editing. **Xiang Ren:** Data curation, Formal analysis. **Hongmin Ma:** Formal analysis. **Dawei Fan:** Formal analysis. **Dan Wu:** Funding acquisition, Formal analysis, Project administration. **Qin Wei:** Funding acquisition, Formal analysis. **Huangxian Ju:** Formal analysis.

## Declaration of competing interest

The authors declare that they have no known competing financial interests or personal relationships that could have appeared to influence the work reported in this paper.

## Data availability

No data was used for the research described in the article.

## Acknowledgments

This work was supported by the Young Taishan Scholars Program of Shandong Province (tsqn201909124), the National Natural Science Foundation of China (22274063), the Project of “20 items of University” of Jinan (2019GXRC018), the Innovation Team Project of Colleges and Universities in Jinan (2019GXRC027). All of authors express their sincere thanks.

## Appendix A. Supplementary data

Supplementary data to this article can be found online at https://doi.org/10.1016/j.aca.2023.341541.

## References

[1] L. Huang, Z. Liang, F. Zhang, H. Luo, R. Liang, F. Han, Z. Wu, D. Han, J. Shen, L. Niu, Upconversion $NaYF_4$:Yb/Er–$TiO_2$–$Ti_3C_2$ heterostructure-based near-infrared light-driven photoelectrochemical biosensor for highly sensitive and selective d-serine detection, Anal. Chem. 94 (2022) 16246–16253.

[2] W. Xiao, W. Xu, W. Huang, Y. Zhou, Z. Jin, X. Wei, J. Li, Bismuth-based $BiOBr_xI_{1-x}$/$Ti_3C_2$ MXene Schottky nanocomposites for $Hg^{2+}$ photoelectrochemical sensors, ACS Appl. Nano Mater. (2022).

[3] J. Yang, W. Li, L. Guo, F. Luo, B. Qiu, Z. Lin, L. Wang, Highly sensitive photoelectrochemical biosensor for MicroRNA-21 based on a dumbbell-shaped heterostructure AuNRs@end-$TiO_2$ combined with carbon dots as photosensitizers and duplex-specific nuclease-assisted signal amplification, Anal. Chem. 94 (2022) 13575–13581.

[4] T. Hou, N. Xu, X. Song, L. Yang, F. Li, Label-free homogeneous photoelectrochemical aptasensing of $VEGF_{165}$ based on DNA-regulated peroxidase-mimetic activity of metal-organic-frameworks, Chin. Chem. Lett. 34 (2023), 107907.

[5] F. You, J. Wei, Y. Cheng, Z. Wen, C. Ding, N. Hao, K. Wang, Selective and sensitive photoelectrochemical aptasensor for streptomycin detection based on $Bi_4VO_8Br$/$Ti_3C_2$ nanohybrids, J. Hazard Mater. 414 (2021), 125539.

[6] L. Ge, Q. Hong, H. Li, C. Liu, F. Li, Direct-laser-writing of metal sulfide-graphene nanocomposite photoelectrode toward sensitive photoelectrochemical sensing, Adv. Funct. Mater. 29 (2019), 1904000.

[7] W.-W. Zhao, J.-J. Xu, H.-Y. Chen, Photoelectrochemical DNA biosensors, Chem. Rev. 114 (2014) 7421–7441.

[8] W.-w. Zhan, Q. Kuang, J.-z. Zhou, X.-j. Kong, Z.-x. Xie, L.-s. Zheng, Semiconductor@Metal–Organic framework core–shell heterostructures: a case of ZnO@ZIF-8 nanorods with selective photoelectrochemical response, J. Am. Chem. Soc. 135 (2013) 1926–1933.

[9] Z. Wen, W. Zhu, F. You, R. Yuan, L. Ding, N. Hao, J. Wei, K. Wang, Ultrasensitive photoelectrochemical aptasensor for carbendazim detection based on in-situ constructing Schottky junction via photoreducing Pd nanoparticles onto CdS microsphere, Biosens. Bioelectron. 203 (2022), 114036.

[10] Y. Zhao, J. Xiang, H. Cheng, X. Liu, F. Li, Flexible photoelectrochemical biosensor for ultrasensitive microRNA detection based on concatenated multiplex signal amplification, Biosens. Bioelectron. 194 (2021), 113581.

[11] D.-N. Chen, G.-Q. Wang, L.-P. Mei, J.-J. Feng, A.-J. Wang, Dual II-scheme nanosheet-like $Bi_2S_3$/$Bi_2O_3$/$Ag_2S$ heterostructures for ultrasensitive PEC aptasensing of aflatoxin B1 coupled with catalytic signal amplification by dendritic nanorod-like Au@Pd@Pt nanozyme, Biosens. Bioelectron. 223 (2023), 115038.

[12] H. Du, X. Ma, N. Li, L. Yang, G. Yang, Q. Li, Q. Wang, Exceptional visible-light photoelectrocatalytic activity of dual Z-scheme Bi@BiOI-$Bi_2O_3$/$C_3N_4$ heterojunction for simultaneous remediation of Cr(VI) and phenol, Colloid Interface Sci. 640 (2023) 132–143.

[13] Q. Fu, C. Wang, J. Chen, Y. Wang, C. Li, Y. Xie, P. Zhao, J. Fei, $BiPO_4$/BiOCl/g-$C_3N_4$ heterojunction based photoelectrochemical sensing of dopamine in serum samples, Colloid. Surface. 656 (2023), 130456.

[14] A.-M. Chang, Y.-H. Chen, C.-C. Lai, Y.-C. Pu, Synergistic effects of surface passivation and charge separation to improve photo-electrochemical performance of BiOI nanoflakes by Au nanoparticle decoration, ACS Appl. Mater. Interfaces 13 (2021) 5721–5730.

[15] H. Wang, B. Zhang, Y. Tang, C. Wang, F. Zhao, B. Zeng, Recent advances in bismuth oxyhalide-based functional materials for photoelectrochemical sensing, TrAC, Trends Anal. Chem. 131 (2020), 116020.

[16] Y. Luo, X. Tan, D.J. Young, Q. Chen, Y. Huang, D. Feng, C. Ai, Y. Mi, A photoelectrochemical aptasensor for the sensitive detection of streptomycin based on a $TiO_2$/BiOI/BiOBr heterostructure, Anal. Chim. Acta 1115 (2020) 33–40.

[17] Y. Wang, Q. Liu, J. Wei, Z. Dai, L. Ding, R. Yuan, Z. Wen, K. Wang, Visible light-driven photoelectrochemical ampicillin aptasensor based on an artificial Z-scheme constructed from $Ru(bpy)_3^{2+}$-sensitized BiOI microspheres, Biosens. Bioelectron. 173 (2021), 112771.

[18] J.-H. Zhu, Y.-G. Feng, A.-J. Wang, L.-P. Mei, X. Luo, J.-J. Feng, A signal-on photoelectrochemical aptasensor for chloramphenicol assay based on 3D self-supporting AgI/Ag/BiOI Z-scheme heterojunction arrays, Biosens. Bioelectron. 181 (2021), 113158.

[19] M. Wu, M. Dong, Z.M. El-Bahy, T. Jing, G.A.M. Mersal, J. Tian, H. Qi, D. Shi, N. Naik, V. Murugadoss, M.M. Ibrahim, M. Huang, Z. Guo, Preparation of Bi/BiOBr sensitized titania nanorod arrays via a one-pot solvothermal method and construction of kanamycin photoelectrochemical aptasensors, Dalton Trans. 51 (2022) 8279–8289.

[20] L. Xu, X. He, J. Dong, P. Yan, F. Chen, J. Zhang, H. Li, A photoelectrochemical aptasensor for sensitively monitoring chloramphenicol using plasmon-driven AgNP/BiOCl composites, Analyst 145 (2020) 7695–7700.

[21] A.L. Greenaway, S. Ke, T. Culman, K.R. Talley, J.S. Mangum, K.N. Heinselman, R. S. Kingsbury, R.W. Smaha, M.K. Gish, E.M. Miller, K.A. Persson, J.M. Gregoire, S. R. Bauers, J.B. Neaton, A.C. Tamboli, A. Zakutayev, Zinc titanium nitride semiconductor toward durable photoelectrochemical applications, J. Am. Chem. Soc. 144 (2022) 13673–13687.

[22] Y. Bai, D. Leng, T. Feng, X. Kuang, D. Fan, X. Ren, Y. Li, Q. Wei, H. Ju, A split-type photoelectrochemical immunosensor based on a high-performance $In_2O_3$/$BiVO_4$ photoelectrode modulated by a ZIF-8 protective layer, Sensor. Actuator. B Chem. 382 (2023), 133479.

[23] Q. Zhou, H. Chen, K. Wang, H. Zhang, L. Pan, H. Zheng, Y. Zhou, Z. Hu, Z. Peng, J. Wan, B. Wang, Photoelectrochemical immunosensor for archaeological silk microtrace detection based on tailored monoclonal antibody and ZnO nanowires array, Sensor. Actuator. B Chem. 374 (2023), 132804.

[24] X. Liu, Y. Zhao, F. Li, Nucleic acid-functionalized metal-organic framework for ultrasensitive immobilization-free photoelectrochemical biosensing, Biosens. Bioelectron. 173 (2021), 112832.

[25] P. Miao, M. Hao, C. Li, W. Wang, S. Ge, X. Yang, B. Geng, B. Ding, J. Zhang, M. Yan, Integrating $Ti_3C_2$/$MgIn_2S_4$ heterojunction with a controlled release strategy for split-type photoelectrochemical sensing of miRNA-21, Anal. Chim. Acta 1215 (2022), 339990.

[26] X. Zhang, J. Zhang, Y. Gao, J. Yan, W. Song, Controllable signal molecule release from Au NP-gated MSNs for photocathodic detection of ultralow level AβO, Chem. Commun. 58 (2022) 839–842.

[27] D. Leng, J. Zhao, X. Ren, R. Xu, L. Liu, X. Liu, Y. Li, Q. Wei, $MoSe_2$/CdSe heterojunction destruction by cation exchange for photoelectrochemical immunoassays with a controlled-release strategy, Anal. Chem. 93 (2021) 10712–10718.

[28] N. Zhang, D. Leng, Y. Wang, Z. Ru, G. Zhao, Y. Li, D. Zhang, Q. Wei, Split-type photoelectrochemical/visual sensing platform based on $SnO_2$/$MgIn_2S_4$/$Zn_{0.1}Cd_{0.9}S$ composites and Au@$Fe_3O_4$ nanoparticles for ultrasensitive detection of neuron specific enolase, Anal. Chem. 94 (2022) 15873–15878.

[29] R. Xu, L. Liu, X. Liu, Y. Li, R. Feng, H. Wang, D. Fan, D. Wu, Q. Wei, Novel electron donor encapsulation assay based on the split-type photoelectrochemical interface, ACS Appl. Mater. Interfaces 12 (2020) 7366–7371.

[30] Y. Gao, Y. Zeng, X. Liu, D. Tang, Liposome-mediated in situ formation of type-I heterojunction for amplified photoelectrochemical immunoassay, Anal. Chem. 94 (2022) 4859–4865.

[31] X. Li, X. Wang, L. Zhang, J. Gong, High-throughput signal-on photoelectrochemical immunoassay of lysozyme based on hole-trapping triggered by disintegrating bioconjugates of dopamine-grafted silica nanospheres, ACS Sens. 3 (2018) 1480–1488.

[32] J.H. Kim, T. Lim, J.Y. Park, A. Ma, H. Jung, H.Y. Kim, S.K. Cho, H. Yoon, K.M. Nam, Understanding and improving photoelectrochemical performance of $Bi_2O_3$/$Bi_2S_3$ composite, New J. Chem. 43 (2019) 11893–11902.

[33] C. Hong, Y.-I. Kim, J.H. Seo, J.H. Kim, A. Ma, Y.J. Lim, D. Seo, S.Y. Baek, H. Jung, K.M. Nam, Comprehensive study of the growth mechanism and photoelectrochemical activity of a $BiVO_4$/$Bi_2S_3$ nanowire composite, ACS Appl. Mater. Interfaces 12 (2020) 39713–39719.

[34] D. He, X. He, K. Wang, M. Chen, J. Cao, Y. Zhao, Reversible stimuli-responsive controlled release using mesoporous silica nanoparticles functionalized with a smart DNA molecule-gated switch, J. Mater. Chem. 22 (2012) 14715–14721.

[35] Q. Zhou, Y. Lin, J. Shu, K. Zhang, Z. Yu, D. Tang, Reduced graphene oxide-functionalized FeOOH for signal-on photoelectrochemical sensing of prostate-specific antigen with bioresponsive controlled release system, Biosens. Bioelectron. 98 (2017) 15–21.

[36] B. Zhang, L. Lu, Q. Hu, F. Huang, Z. Lin, ZnO nanoflower-based photoelectrochemical DNAzyme sensor for the detection of $Pb^{2+}$, Biosens. Bioelectron. 56 (2014) 243–249.

[37] X. Shi, P. Wang, W. Li, Y. Bai, H. Xie, Y. Zhou, L. Ye, Change in photocatalytic NO removal mechanisms of ultrathin BiOBr/BiOI via $NO_3$– adsorption, Appl. Catal. B Environ. 243 (2019) 322–329.

[38] X. Lu, Q. Li, L. Wang, W. Jiang, R. Luo, M. Zhang, C. Cui, Z. Tian, G. Zhu, Fabrication of one dimensional hierarchical $WO_3$/BiOI heterojunctions with enhanced visible light activity for degradation of pollutants, RSC Adv. 11 (2021) 16608–16618.

[39] W. Li, X. Geng, F. Xiao, G. An, D. Wang, FeII/FeIII doped Bi/BiOBr hierarchical microspheres as a highly efficient catalyst for degradation of organic contaminants at neutral pH: the role of visible light and $H_2O_2$, ChemCatChem 9 (2017) 3762–3771.

[40] L. Lin, M. Huang, D. Chen, BiOBr/BiOI Photocatalyst Based on Fly Ash Cenospheres with Improved Photocatalytic Performance, Molecules, 2016.

[41] X. Shi, P. Wang, L. Lan, S. Jia, Z. Wei, Construction of $BiOBr_xI_{1-x}$/MXene $Ti_3C_2T_x$ composite for improved photocatalytic degradability, J. Mater. Sci. Mater. Electron. 30 (2019) 19804–19812.

[42] F. Xiao, J. Xu, Z. Wang, S. Jiang, Q. Zhang, L. Wang, Construction of oxygen vacancy modified Bi/BiOI nanocomposite with improved photocatalytic activity for microcystin-LR degradation, J. Mater. Sci. Mater. Electron. 31 (2020) 17003–17012.

[43] D. Yuan, L. Huang, Y. Li, Y. Xu, H. Xu, S. Huang, J. Yan, M. He, H. Li, Synthesis and photocatalytic activity of g-$C_3N_4$/BiOI/BiOBr ternary composites, RSC Adv. 6 (2016) 41204–41213.

[44] Z. Liu, H. Ran, B. Wu, P. Feng, Y. Zhu, Synthesis and characterization of BiOI/BiOBr heterostructure films with enhanced visible light photocatalytic activity, Colloid. Surface. 452 (2014) 109–114.

[45] T. Wu, J. Feng, S. Zhang, L. Liu, X. Ren, D. Fan, X. Kuang, X. Sun, Q. Wei, H. Ju, A self-powered photoanode-supported photoelectrochemical immunosensor for CYFRA 21-1 detection based on $In_2O_3$/$In_2S_3$/$CdIn_2S_4$ heterojunction, Biosens. Bioelectron. 169 (2020), 112580.